Preprint submitted to Journal of Composite Materials

On the Mechanical Performance of Non-crimp Fabric H-Shaped Adhesively Bonded Joints

K.I. Tserpes[1,*], Jacques Cinquin[2] and Sp. Pantelakis[1]

[1]*Laboratory of Technology & Strength of Materials*
Department of Mechanical Engineering & Aeronautics
University of Patras, Patras 26500, GREECE

[2]*European Aeronautic Defense and Space Company*
Innovation Works (EADS / IW)
12 rue Pasteur, 92150 Suresnes, FRANCE

ABSTRACT

Adhesive bonding is contemplated as an alternative method to mechanical fastening for joining composite aerostructures. Ongoing research in this area is focused on the development of new bonding techniques and joining elements. In this paper, the mechanical performance of the novel non-crimp fabric (NCF) **H**-shaped adhesively bonded joints subjected to tension, shear and 4-point bending loading conditions was investigated by both experimental tests and numerical modeling. The **H** profiles were manufactured by employing the preforming and injection moulding methods, while bonding of the assembled parts was carried out using a novel stepwise procedure which leads to a high bonding quality. Investigation was conducted by means of mechanical testing and a mesomechanical model based on the FE method and the progressive damage modeling approach. In the model, both adhesive failure (debonding) and failure of the NCF material is considered. In the tension and shear load-cases, the joint failed due to extensive debonding attributed to adhesive shearing, while in the 4-point bending load-case, due to failure of the **H** element. In all three load-cases, the experimental and numerical results compare well thus, providing establishment of the numerical model in simulating the performance of textile structural parts. Lastly, the effort presented herein is rated as successful since new adhesive bonded joints of high mechanical performance are proposed.

KEY WORDS: Adhesive joints, Non-crimp fabrics, Debonding, Finite element analysis (FEA), Injection moulding, Progressive damage modeling.

[*]Corresponding author. Tel.: +30 2610 969498, Fax: +30 2610 997190, e-mail: kit2005@mech.upatras.gr

INTRODUCTION

While the goal of introducing composite materials in aircraft structures has been partially achieved, through the extensive use of CFRP laminates in military and civil aircrafts, latest major developments are still favoring the use of composite materials in order to further reduce weight, subsequent fuel consumption and associated pollution. In the frame of this effort, various technical challenges, which up to now have been left aside, must be faced. Perhaps the most important of these challenges is *boltless joining* [1].

Conventional mechanical fastening for composite aerostructures although optimized today introduces a weight penalty due to the thickness increase of the assembled components near the bolts and the additional weight of bolts. In order to optimize design of composite bolted joints in a way allowing to reduce weight several experimental [2-4] and numerical [5-8] investigations have been conducted. However, due to the complexity of composite materials, no significant improvement has been made and the research community has directed the interest to indirect solutions, such as cost-effective reinforcement of existing mechanical fastening concepts and adhesive bonding. For establishing adhesive bonding as a reliable joining method, the ability of bonded joints to efficiently transfer load between assembled parts must be fully ensured. This pertains equally to the integrity of the joining element and bondline. As bonded joints are designed such that the load is transferred through shear, normal tensile loads arise in specific areas of the composite joining element. In bonded joints between traditional composite laminates such loads may lead to delamination in either the joining element or the assembled parts. Therefore, for this kind of applications, new composite materials with enhanced through thickness properties must be employed. Such materials are the 2D and 3D woven fabrics and the non-crimp fabric (NCF) composites. Understanding of the precise mechanical behavior of these materials is still in progress. On the other hand, integrity of the bondline depends on a variety of geometrical and material parameters. Geometry optimization of the bonded joint is required to keep the maximum shear loads as low as possible [9]. Adhesives with specific chemical compositions possessing enhanced shear strength are also proposed [10,11]. Beyond any doubt, quality of the bondline plays an important role since imperfect bonding may cancel all aforementioned improvements [12-13].

The work reported in the literature on composite joining profiles is limited and concentrated on the **T**-joints. Mainly, the mechanical behavior of transversely stitched **T**-joints [14,15] and **T**-joints for marine applications [16,17] has been studied by employing

both experiments and numerical analysis. In a recent paper, Chen et al. [18] predicted delamination of braided composite **T**-piece specimens using cohesive models. In none of these studies **T**-shaped profiles have been used as joining elements to adhesively bond different parts. The first systematic research on the use of composite profiles as joining elements in adhesively bonded joints was conducted in the frame of a European research project evolved from 2006 to 2009 [19]. There, a material driven design concept for modular **Pi**-, **H**-, **L**- and **T**-shaped bonded joints made of woven fabric material was developed. The research pertained to the development of new manufacturing techniques for the woven fabric profiles, new bonding techniques with controlled bonding quality as well as the optimization of the profiles with regard to the integrity of the composite material and the ability of the bondline to transfer specific levels of load.

In the present paper, the research conducted on the manufacturing and characterization of the **H**-shaped joints is described. Despite the similarities of the **H**-element with the classical double-lap shear joint configuration, there are certain advantages that enhance potentiality of the H-based concept. For instance, the H-element can be manufactured very easily and cost effectively by pultrusion. Also, in combination with the other joining profiles it introduces a modular joining concept which can be used to adhesively join several structural parts easily without modifying the configuration of the structure as happens in the double-lap shear joint, which implies the bonding of three parts to bridge load between two different directions. A gain in the mechanical performance is also expected to occur due to the larger overlap area between the bonded parts.

This paper is divided into 6 main sections. Following this introduction, the problem is shortly defined in Section 2. In Section 3, materials, manufacturing, bonding and experimental set-up are described. In Section 4, we provide a description of numerical modeling. Experimental and computed results for each load-case are presented and discussed in a comparative way in Section 5. Finally, we conclude the article in Section 6.

PROBLEM STATEMENT

The geometry considered represents an **H**-shaped joining element, schematically shown in Fig.1, used to adhesively join two composite laminated plates. The goal of this work is to study the performance of the joint under different loading conditions. The study is focused on both the strength of the joint's material and the effectiveness of adhesive bonding in transferring load between the assembled plates. The loading conditions considered are:

tension, shear and 4-point bending. Schematics of the loading conditions along with the dimensions of the joint in each load-case are shown in Fig.2.

EXPERIMENTAL

Materials

The NCF material was manufactured from the high resistance HTS carbon fibres stacked in the quasi-isotropic lay-up: $-45°/0°/45°/90°/V$ where V is a veil placed at the surface to bond the different layers of the preform together. The global area weight of the preform is 516 g/m² and the area weight of the veil is 6 g/m². The symmetric NCF lay-up: $V/45°/0°/-45°/90°$ was also used in order to produce equilibrated preforms. The lay-up of the **H**-shaped profile is described in Fig.3. The RTM6 resin used is a mono component epoxy system largely used in aerospace RTM part production. The laminated plates are made from the IMS 24K/977-2 prepreg following the quasi-isotropic lay up: $[(0°/45°/-45°/90°)_3]_S$. The thickness of the plates is 6 mm. Their front edge inserted in the **H** was machined with a radius of 3 mm. For the bonding, the supported EA9695 epoxy film adhesive with a nominal thickness of 195 μm was used. Such an adhesive has the edge on paste adhesive because it allows for the application of pressure during polymerisation phase, enables better control of bondline thickness and also possesses better mechanical performance. The material properties of the adhesive are listed in Table 1.

Manufacturing of the H Joining Element

Manufacturing of the **H** profile was carried out in two stages: (a) manufacturing of the **H** preform, and (b) production of the final **H** profile using the RTM technology. In the preforming process, initially the binder of the NCF material is activated through heating up to the temperature of 120°C and cooling down to 80°C in order to be used for the fixation of the different layers in manageable preforms. Given the geometry of the preforms, the shaping tools to be used in the performing process were determined and produced. Finally, the preforming concept is applied by means of the process schematically illustrated in Fig.4. The produced **H** preform is shown in Fig.5.

After created, the carbon-fibre preform was elaborated with NCF and epoxy resin. Different layers were bonded together by means of a polyamide veil placed between by heating above melting temperature of the polyamide. A special mould was developed for the injection of the **H** profile. The choice of the final polymerisation temperature is flexible

ranging between 150°C to 200°C. Details about the preform and RTM processes can be found in [20].

Bonding

Bonding of the parts was accomplished following the stepwise procedure schematically represented in Fig.6: (1) injection of the **H** preform by the RTM process and partially curing to allow for further hot forming process, (2) surface preparation, deposition of the adhesive film and positioning of parts, and (3) hot forming of the **H** element with pressure and temperature cycle, adhesive polymerization and final **H** polymerization. The polymerization temperature falls within the range 120°C-175°C. Fig.7 shows positioning of adhesive and laminated plates in the **H** profile. By carefully deposing the adhesive on the entire internal area of the H element before positioning of the parts, an almost perfect bondline of uniform thickness with no voids is finally achieved. This is the main advantage of this procedure over the methods based on the coerced adhesive flow such as the insertion squeeze flow method [12,13]. The expected excellent bonding quality was ascertained in all assembled specimens using ultrasonic C-scan inspection.

Mechanical Testing

To characterize the mechanical performance of the **H** joint, experimental tests for the load-cases described in Fig.2 were conducted. For each load-case, three specimens were tested. Tension and 4-point bending tests were conducted using an MTS machine with 500 kN capacity, while shear tests using an INSTRON machine with 300 kN capacity. The tension test was conducted with a speed of 0.1 mm/min, the shear test with a speed of 0.2 mm/min and the 4-point bending test with a speed of 5 mm/min. During mechanical tests, the strain of the samples were monitored on one edge of the sample using the ARAMIS system [21]. This system offers a non-contact determination of deformation and strain using 3D video correlation methods and high-resolution digital CCD cameras. Clearly visible area patterns, which are deformed along with the object, are created by painting small black areas of different sizes on white basic colors in order to achieve a good contrast on the object's surface. The deformation of the sample under different load conditions is recorded by the CCD cameras and evaluated using digital image processing. The outcome is the 3D strain field of the specimen.

NUMERICAL SIMULATION

To date, both analytical and numerical models have been adopted for predicting the behavior of adhesively bonded joints. Most of the analytical models are two-dimensional, thus neglecting stresses across the width direction and assume a linear elastic behavior for both the adherents and adhesive [22]. Therefore, they are unable to predict how debonding reflects to the overall behavior of complex 3D bonded joints and consider failure of the adherents. In addition, most of the analytical models are too complicated to be integrated in FE models. Numerical models, mainly based on the FE method, have been focused on the accurate prediction of debonding initiation and progression by adopting very detailed FE meshes and targeting techniques based on fracture mechanics. Two of the most popular techniques in this area are the virtual crack closure technique [23] and cohesive zone modeling [24]. However, these techniques demand for the debonding initiation location to be specified. This requirement makes these techniques inapplicable in cases where parameters, such as complicated geometry and loading or the presence of defects, do not allow to know a priori the failure initiation location.

Nevertheless, the scope of the present work was not to study in detail the failure mechanisms that may develop in the joint but to assess the joint's overall mechanical performance in order to examine the feasibility of the adhesive modular joining concept [19]. To this end, instead of using one of the detailed methods in the previous paragraph, a mesomechanical model [25] based on the progressive damage modeling method was adopted. The model considers debonding initiation and progression as well as failure in the composite material of the **H**. Although not focused on the precise prediction of debonding initiation, it can however take into account how debonding initiation and progression influence the overall performance of the joint. In addition, the ability of progressive damage modeling method to predict failure initiation, wherever it takes place, and monitor failure progression makes it an ideal complement to experiments because it can be directly compared to any type of experimental result, used for further evaluation of the experimental findings and shed light in damage details which cannot be explained experimentally. The mesomechanical model has been successfully used in simulating adhesively bonded joints in [12,13]. In brief, the model comprises the steps of:

- definition of the RVE of the woven fabric composite,
- characterization of the mechanical behavior of the RVE using local homogenized progressive damage modeling,

- development of the FE model of the joint,
- assignment of the behavior of the RVE to the elements of the FE model and implementation of progressive damage modeling to simulate the global mechanical performance of the joint.

More details can be found in [25].

Characterization of the NCF Multi-layers

In [25], the mechanical behavior of the NCF HTS/RTM6 dual layers $0^\circ/90^\circ$ and $45^\circ/-45^\circ$ was fully characterized. Taking into advantage that the quad-layers comprising the **H** profile is a synthesis of these dual-layers, in order to avoid redoing of the characterization procedure, a simplified engineering mechanics approach was proposed in [13] for evaluating the behavior of the quad-layers based on the behavior of the dual-layers. For brevity's sake, the approach will not be presented again here but only the outcome which are the equations describing the stiffness E_3 and tensile strength S_3 of the quad-layers as functions of the stiffnesses and strengths of the dual-layers (index 1 refers to $0^\circ/90^\circ$ and 2 to $45^\circ/-45^\circ$)

$$E_3 = \frac{1}{2}E_1 + \frac{1}{2}E_2, \tag{1}$$

$$S_3 = \left(\frac{E_1}{E_2}\right)\cdot\frac{S_2}{2} + \frac{S_2}{2} + \left(S_1 - \frac{E_1}{E_2}S_2\right). \tag{2}$$

Given the stiffnesses and strengths of the dual-layers, as evaluated in [25], and by assuming that the above procedure stands for any type of loading, the corresponding properties of the quad-layers were derived using Eqs. (1) and (2). The evaluated homogeneous material properties of the quad-layers are listed in Table 2. *X*, *Y* and *Z* directions are described in Fig.1. Note that for simplification reasons, a linear variation of the stiffnesses was assumed. This assumption is not far from reality since all the stress-strain curves derived in [25] are almost linear.

FE Model

The 3D FE model of the joint was developed using the ANSYS FE code [26]. The assembled parts and constituents of the composite **H** element were modeled separately using the 3D

structural solid SOLID185 element defined by eight nodes with three degrees of freedom per node. The front-view of the FE mesh of the joint is shown in Fig.8. As shown, each of the NCF L- and U-layers was modeled by a separate row of elements in order to be able to assign to the elements the corresponding material properties listed in Table 2 and also to be treated separately in the modules of failure analysis and material property degradation. The same stands also for the adhesive. In order to minimize the required computational effort, a coarse mesh has been adopted. This leads to elements of high aspect ratio and increased numerical error. While at non critical areas the numerical error is not expected to influence the simulation, at critical areas it is expected to influence the failure initiation load which reflects to an alteration in specimen's failure load within the accepted range of 5%.

For each load-case, the exact dimensions of the specimens shown in Fig.2 were modeled. Tension load was simulated by fully constraining one end of the insert and applying an incremental axial displacement at the opposite end. Shear load was simulated by fully constraining the transverse side of the cantilever of the insert and applying an incremental displacement at the corresponding opposite side. Finally, 4-point bending was simulated by applying an incremental normal displacement through-width of the insert at the nodes located under the upper forces shown in Fig.2(c) and at the same time constraining the nodes under the lower forces.

Failure Analysis and Material Property Degradation

At each load step, failure analysis and material property degradation are performed consecutively both at the NCF material and the adhesive. Element failures are predicted by comparing stresses with material strengths at each direction (Maximum Stress failure criterion). As soon as failure is reached, the stiffnesses of the failed elements are degraded according to the severity of failure. Failure in the fibers direction is assumed to be catastrophic and thus, all stiffnesses are degraded in order to totally disable the elements from carrying load. On the contrary, when failure is predicted in the directions transverse and normal to the fibers, the corresponding stiffnesses are degraded such as to disable the load-carrying capability only at the specific directions. Material property degradation rules are depicted in Table 3. The coordinate system they refer to is defined in Fig.1.

Prediction of debonding is fundamental since it is expected to be the primary failure mode of the **H** joint. Debonding is mainly due to shear failure of the adhesive between the **H**-legs and insert caused by large shear stresses. Secondary debonding may occur due to tensile

fracture owing to large normal tensile axial stresses developed between insert's head and **H**-slots. The afore-mentioned failures are respectively predicted using the following two criteria

$$\tau_{\max} = \frac{\sigma_1 - \sigma_3}{2} \geq \tau_a \tag{3}$$

$$\sigma_{ay} \geq S_a^T \tag{4}$$

where $\tau_{\max}$ is the maximum shear stress at the adhesive, σ_1, σ_3 are the maximum and minimum principal stresses, respectively, and σ_{ay} is the normal axial stress at the loading direction. τ_a is the shear strength of the adhesive and S_a^T the tensile strength taken twice the τ_a. As soon as failure is predicted in an element of the adhesive, its stiffness is totally degraded to simulate debonding by totally disabling the element to transfer load between the insert and the **H**. Plasticity of the adhesive has not been taken into account.

The failure criteria (3) and (4) although not able to provide a precise prediction for debonding initiation and progression as a cohesive zone model or a fracture mechanics approach do so, they can however give accurate simulations about the extent of debonding and its effect on the overall mechanical performance of the joint [12,25] and also to take into account the possible effect of imperfect bonding [13].

EXPERIMENTAL AND NUMERICAL RESULTS

Tension

In Fig.9, the experimental load-grip displacement curves are compared with the numerical curve for the tension load-case. The comparison reveals a good agreement regarding both the failure load (mean experimental value: 98368N vs. numerical value: 94540N) and the joint stiffness. The small deviation between measured and predicted stiffnesses may be attributed to the role of grips' stiffness and the relative sliding between the grips and specimen's tabs which influence the measurements of grip displacement. Both methods give a slightly non-linear behavior for the joint owing to progressing debonding and localized failures in the composite material.

Illustrated in Fig.10 is the strain contour in the loading direction of the joint, as measured by the ARAMIS system, just before failure. Large deformation, shown in red, is

concentrated in the central part of the joint due to various failures initiated and accumulated there. Early adhesive failure occurred between insert's head and **H**-slots due to large tensile normal stresses. Local failures also appeared in the area between the U-layer, the gusset filler and the resin-rich area due to stiffness discontinuity and manufacturing defects indicated by the dashed circle in the image shown in Fig.11. The latter failures could not be captured by the model since the presence of defects was not considered; however, the early adhesive failure has been accurately simulated as can be seen in Fig.12(a). Final failure of the joint was due to extensive debonding (adhesive shearing) which led to pull-out of the insert from the **H** as shown in Fig.11. The large shear stresses developed between the **H** and the adhesive caused also some failures on the surface of the composite insert in contact with the adhesive layer. The main failure mechanism of the joint was captured by the model as reveals the predicted evolution of debonding shown in Fig.12(b). Moreover, the correct prediction of the failure load revealed in Fig.9 is a hint that initiation and progression of failure has been correctly simulated by the model.

To evaluate the load-carrying capability of the **H**-shaped joint, its tensile response is compared to that of the double-lap shear joint. For the comparison, the configuration of the double-lap shear joint studied in [12] is considered. A direct comparison of the failure loads is not possible since the joints, although are made from the same NCF material, they do not have the same dimensions. However, a comparison in terms of the apparent adhesive shear stress defined as the ratio of the maximum load sustained by the joint to the total adhesive's area is useful. The calculation gives 7.2 MPa vs. 23.42 MPa indicating a clear advantage of the double-lap shear joint. However, this is only an indication since many manufacturing, assembling and material parameters, that differ between the two cases, may play a role in the behavior of the joints. On the other hand, an advantage of the **H**-joint comes from the observed failure mechanisms. Whereas all **H**-joint specimens subjected to tension failed due to adhesive cohesive failure, in some of the double-lap shear joint specimens fracture of the boundary layer composite of the joining element was also observed. In addition, there are also some clear manufacturing and modular joining advantages of the **H**-shaped joint mentioned in the introduction of the paper.

Shear

In Fig.13, the experimental load-grip displacement curves are compared with the numerical curve for the shear load-case. A good agreement is achieved between the two methods regarding the failure load (mean experimental value: 48320N vs. numerical value 43130N),

joint stiffness and sustained deformation. The deviation between the two experimental curves and the numerical curve beyond 0.8 mm is mainly attributed to the coarse mesh of the adhesive adopted in the FE model. Specifically, the choice of one element through thickness has a certain effect in the calculation of shear stress, the prediction of shear failure and the simulation of material property degradation, thus devitalizing the ability of the model to capture the actual slow progression of adhesive's shear failure when the joint is subjected to shear. A possible reason could also be the presence of defects which may further degrade the performance of the joint especially at large applied displacements.

Illustrated in Fig.14 is the strain contour in the joint subjected to shear, as measured by the ARAMIS system, just before failure. The contour shows a homogeneous evolution of deformation from positive values at the left loaded side of the joint to negative values at the right restrained side. The deformation of the **H** element, delimited by the green area in the contour, is positive. As for the tension load-case, the joint failed due to extensive debonding (adhesive shearing) which led to pull-out of the insert from the **H** as shown in Fig.15. The large shear stresses developed between the **H** and the adhesive detached the U-layer from the **H** as can be seen in Fig.15.

4-point bending

In Fig.16, the experimental load-transverse displacement curves are compared with the numerical curve for the 4-point bending load-case. A reasonable agreement is achieved regarding the failure load (mean experimental value: 4331 N vs. numerical value: 3900N) and sustained deformation. The observed deviations are mainly attributed to the irregular deformation of the specimen after the first load-peak. Regarding the stiffness, an excellent agreement is initially observed up to the 1100 N indicating the correct model set-up. Thereafter, the two curves start to deviate as the slope of the experimental curve is increasing. This is attributed to the experimental set-up. In Fig.2(c), the two forces pointing upwards correspond to constrains that have been applied in the experiment by the lower steady grip of the machine and in the model by constraining the normal nodal displacement. The two forces pointing downwards have been applied by the moving grip in the experiment and simulated in the model by the implementation of an incremental normal nodal displacement. In both cases, the lower surface of the specimen was free to slide in the transverse directions. However, as the load increases, the friction between the steady grip and the specimen increases thus, progressively restraining sliding of the specimen and increasing the bending rigidity which is translated to the increase in the slope of the experimental curve. Nevertheless, considering the

difficulties of numerical models to capture the 4-point bending rigidity of inhomogeneous structural parts, owing to divergences from the Euler-Bernoulli theory, it can be stated that in the present application the model performed well.

The strain contour in the joint subjected to 4-point bending, as measured by the ARAMIS system just before failure, is illustrated in Fig.17. On the figure, the two parts of the specimen subjected to tension (green color) and compression (blue color) are shown. Failure initiation is localized in the small red area with the largest strain (arrow indication). In Fig.18(a), the predicted deformed shape of the joint at final failure is depicted. Fig.18(b) verifies that the predicted failure initiation took place at the same location as in the experiment. In both the experiment and model failure initiated and progressed in the bondline. Predicted evolution of debonding as a function of applied load is illustrated in Fig.19. After debonding accumulated significantly, the inserts opened the **H** causing final joint failure (explosive in the experiment) as can be seen in Fig.20. Failure of the joint was so severe and sudden that the U-layer was detached together with the insert.

CONCLUSIONS

The goal of this work is to contribute to the effort placed for extending the use of composite materials in aerostructures through the parallel development of new composites of enhanced strength and boltless joining techniques. To this end, reported in the present paper are the development of novel NCF **H**-shaped joining elements for adhesively bonded joints as well as the study of their mechanical performance under the loading conditions of tension (pull-out), 4-point bending and shear using experimental tests and numerical modelling.

The **H** elements were manufactured using the preforming and injection moulding techniques and the bonding of the parts was carried out using a stepwise procedure which leads to a bond of high quality.

In the tension load-case, both the experiments and model showed that the joint failed due to debonding owing to adhesive shearing. Due to debonding the laminated inserts were totally pulled-out from the **H**. In the **H**, some localized failures in the area between the U-layer, the gusset filler and the resin-rich area, owing to stiffness discontinuity and manufacturing defects, were observed. In the shear load-case, both the experiments and model have shown that the joint failed due to debonding owing to adhesive shearing. The U-layer was detached from the **H** together with the insert. In the 4-point bending load-case, the joint failed due to opening of the **H** by the insert after significant accumulation of debonding. Detachment of the U-layer was also observed here. From these findings, it is concluded that

the minimization of manufacturing defects that appear between the U-layer, the gusset filler and the resin-rich area, being responsible for the initiation of local failures and the enhancement in adhesive's strength which in all cases, and especially in tension and shear, will lead to the increase in the joint strength. Nevertheless, the effort for introducing a new joining element for adhesive bonded joints is successful since **H** joining elements of good manufacturing quality and high mechanical performance were developed as also indicated by the small scatter between the three experiments conducted for each load-case.

Between the model and experiments, a reasonable agreement has been achieved in all three cases regarding the predicted failure load, sustained displacement, type and evolution of failure and a satisfactory agreement regarding the joint stiffness. Whichever deviations occurred can be explained by the experimental procedure, while a certain influence is also expected from the coarse FE mesh adopted for the adhesive. From the evaluation of the model predictions for the shear load-case, the need for making specific improvements in the model, such as the use of more than one elements through-thickness of the adhesive, the use of a tailored and more dense the FE mesh in areas where failure initiation is highly probable and the use of more sophisticated failure criteria for predicting adhesive shearing, arise. All aforementioned actions are currently being taken by the authors. By inference, it can be stated that a numerical model able to effectively simulate the mechanical performance of H-shaped bonded joints and thus, aid design through virtual experimentation has been established herein. Furthermore, in all three load-cases the model interpreted the experimental failure analysis by deriving the exact stress-field and shedding light to the failure initiation and progression pattern at the areas where the optical system showed a high strain concentration.

ACKNOWLEDGEMENTS

The current research was conducted within the frame of the EU Project ‘MOJO’ (Modular Joints for Composite Aircraft Components). Financial support provided by the European Commission under contract No 030871 (FP6) is gratefully acknowledged. The authors would like to express their gratitude to the reviewers for their very useful comments that polished the paper.

REFERENCES

[1] Higgins, A. (2000). Adhesive bonding of aircraft structures, *International Journal of Adhesion and Adhesives*, **20**: 367-376.

[2] Ireman, T., Nyman, T. and Hellbom, K. (1993). On design methods for bolted joints in

composite aircraft structures, *Composite Structures*, **25**: 567-578.

[3] Kovács. N., Calado, L. and Dunai, L. (2004). Behaviour of bolted composite joints: experimental study, *Journal of Constructional Steel Research*, **60**: 725-738.

[4] Xiao, Y. and Ishikawa, T. (2005). Bearing strength and failure behavior of bolted composite joints (part I: Experimental investigation), *Composites Science and Technology*, **65**: 1022-1031.

[5] Ireman, T. (1994) Three-dimensional stress analysis of bolted single-lap composite joints, *Composite Structures*, **43**: 195-216.

[6] Camanho, P.P. and Matthews, F.L. (1999). A progressive damage model for mechanically fastened joints in composite laminates, *Journal of Composite Materials*, **33**: 2248-2280.

[7] Tserpes, K.I., Papanikos, P. and Kermanidis, Th. (2001). A three-dimensional progressive damage model for bolted joints in composite laminates subjected to tensile loading, *Fatigue Fract Engng Mater Struct*, **24**: 663-675.

[8] Tserpes, K.I., Labeas, G., Papanikos, P. and Kermanidis Th. (2002). Strength prediction of bolted joints in graphite/epoxy composite laminates, *Composites Part B,* **33**: 521-529.

[9] Papanikos, P., Tserpes, K.I. and Pantelakis, Sp. (2007). Initiation and progression of composite patch debonding in adhesively repaired cracked metallic sheets. *Composite Structures*, **81**: 303-311.

[10] Sturiale, A., Vázquez, A., Cisilino, A. and Manfredi, L.B. (2007). Enhancement of the adhesive joint strength of the epoxy–amine system via the addition of a resole-type phenolic resin, *International Journal of Adhesion and Adhesives*, **27**: 156-164.

[11] Gorbatkina, Y.A., Ivanova-Mumjieva, V.A. and Lebedeva O.V. (2009). Adhesion of modified polymers to fibres: Maxima on adhesive strength-modifier amount curves and the causes of their appearance. *International Journal of Adhesion and Adhesives,* **29**: 9-17.

[12] Llopart, P. Ll., Tserpes, K.I. and Labeas, G.N. (2009). Experimental and numerical investigation of the influence of imperfect bonding on the strength of NCF double-lap shear joints, *Composite Structures*, doi:10.1016/j.compstruct.2009.12.001

[13] Tserpes, K.I., Pantelakis, Sp. and Kappatos, V. (2009). The effect of imperfect bonding on the pull-out behavior of non-crimp fabric Pi-shaped joints. *Computational Materials Science,* doi:10.1016/j.commatsci.2010.05.012.

[14] Stickler, P.B. and Ramulu, M. (2001). Investigation of mechanical behavior of transverse stitched T-joints with PR520 resin in flexure and tension, *Composite Structures*, **52**: 307-314.

[15] Stickler, P.B. and Ramulu, M. (2002). Parametric analyses of stitched composite T-joints by the finite element method, *Materials and Design*, **23**: 751-758.

[16] Dharmawan, F., Thomson, R.S., Li, H., Herszberg, I and Gellert, E. (2004). Geometry and damage effects in a composite marine T-joint, *Composite Structures*, **66**:181-187.

[17] Li, H.C.H., Dharmawan, F., Herszberg, I. and John S. (2006). Fracture behaviour of composite maritime T-joints, *Composite Structures*, **75**:339-350.

[18] Chen, J., Ravey, E., Hallett, S., Wisnom, M. and Grassi, M. (2009). Prediction of delamination in braided composite T-piece specimens, *Composites Science and*

Technology, **69**:2363-2367.

[19] Modular Joints for Aircraft Components (MOJO). Research Project funded by the European Commission within the frame of 6th Framework-Aeronautics and Space. Description of Work, 2006.

[20] Cinquin, J.,Voillaume, H. Stroehlein T and Ruzek, R. (2009). Modular joining of B-stage cured composite element with forming process and film adhesive for structural application. In Proceedings of the ICCM-17 17th International Conference on Composite Materials, 27-31 July 2009, Edinburgh, UK.

[21] ARAMIS system for optical 3D deformation analysis. GOM: Optical Measuring Technique. http://www.gom.com/EN/measuring.systems/aramis/system/system.html.

[22] da Silva, L.F.M., das Neves, P.J.C., Adams, R.D. and Spelt, J.K. (2009). Analytical models of adhesively bonded joints—Part I: Literature survey, *International Journal of Adhesion and Adhesives*, **29**:319-330.

[23] Marannano, G.V., Mistrett,a L., Cirello, A. and Pasta, S. (2008). Crack growth analysis at adhesive–adherent interface in bonded joints under mixed mode I/II, *Engineering Fracture Mechanics*, **75**:5122-5133.

[24] Gustafson, P.A., Waas AM. (2009). The influence of adhesive constitutive parameters in cohesive zone finite element models of adhesively bonded joints, *International Journal of Solids & Structures*, **46**: 2201-2215.

[25] Tserpes, K.I., Labeas, G. (2009). Mesomechanical analysis of composite non-crimp fabric structural parts, *Composite Structures*, **87**:358-369.

[26] ANSYS 11.0 Documentation, 2007.

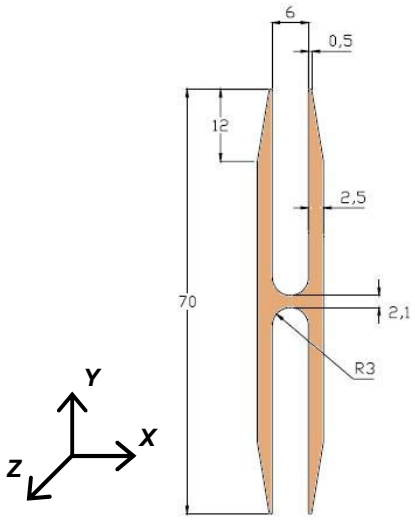

Fig.1: Schematic and dimensions of the **H** joining element.

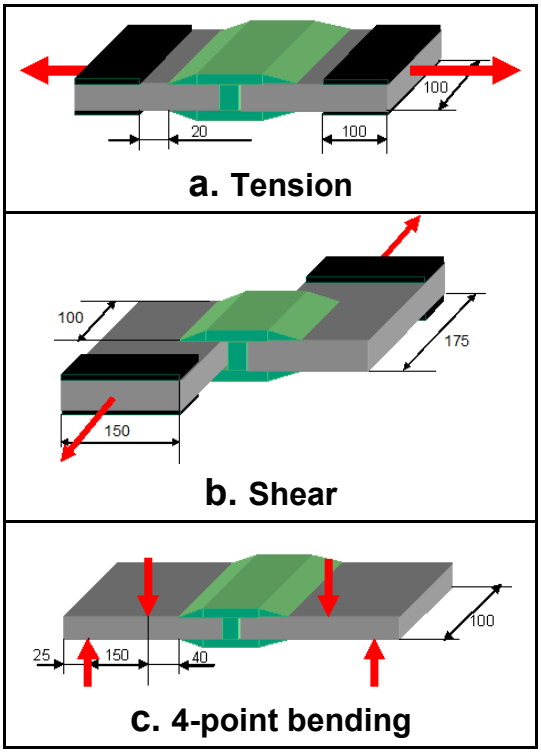

Fig.2: Schematic description of loading conditions and definition of dimensions.

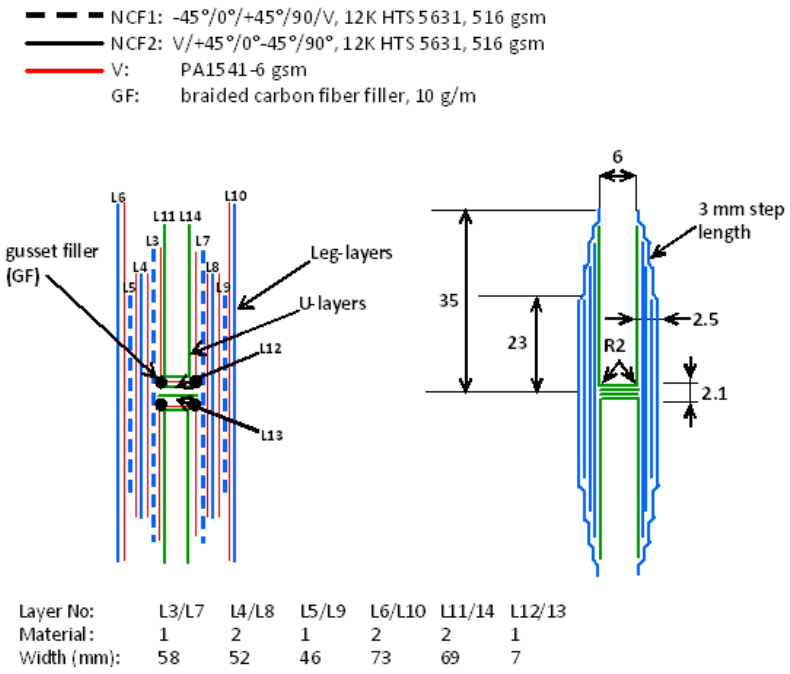

Fig.3: Lay-up of the NCF **H** element.

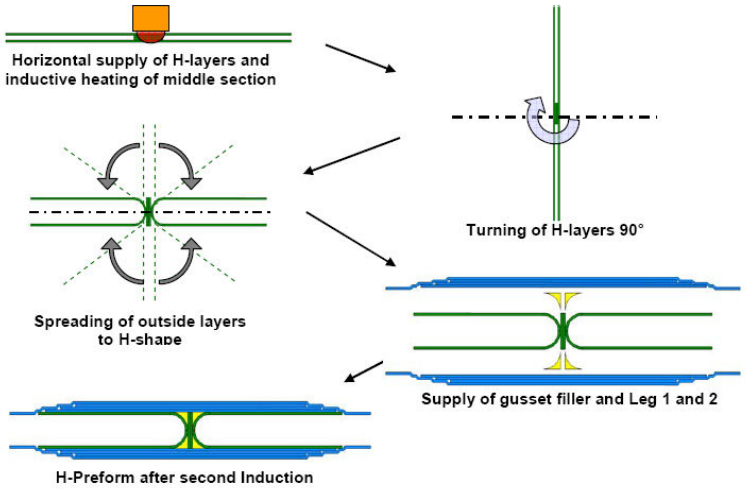

Fig.4: Schematic of the preforming process of the **H** element.

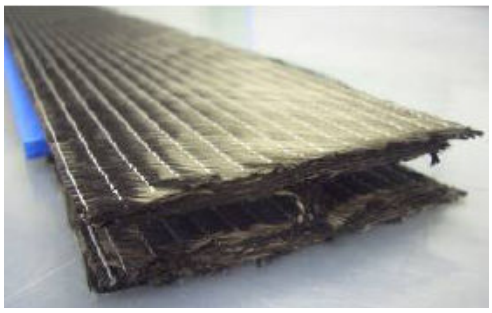

Fig.5: **H** preform.

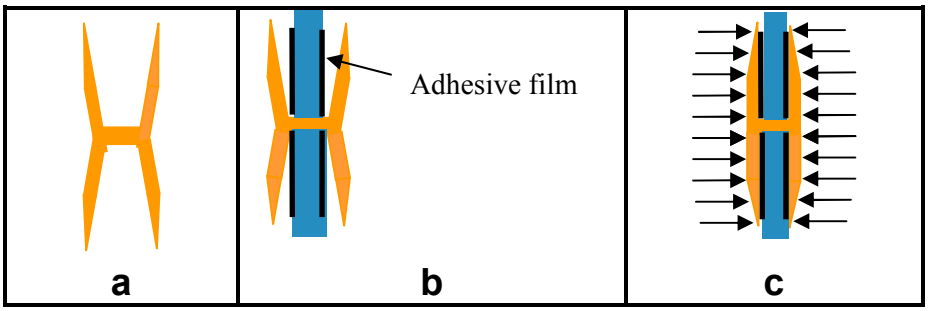

Fig.6: Schematic representation of the stepwise bonding procedure.

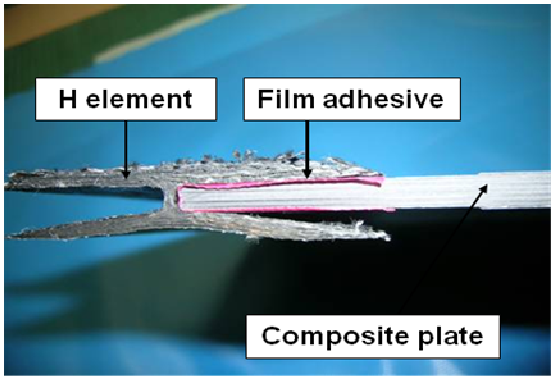

Fig.7: Positioning of the adhesive and laminated plates in the **H** element.

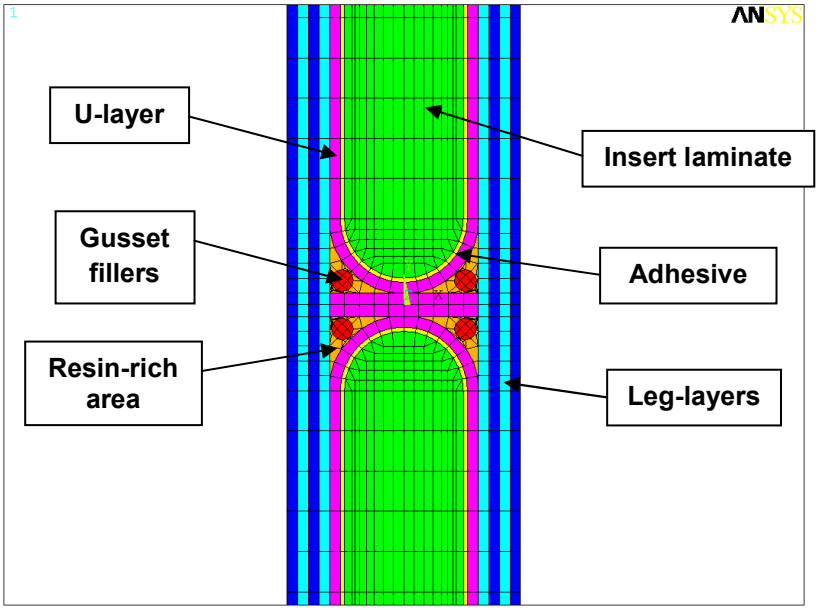

Fig.8: FE mesh of the joint (front-view) and indication of the assembled parts and constituents of the **H** element.

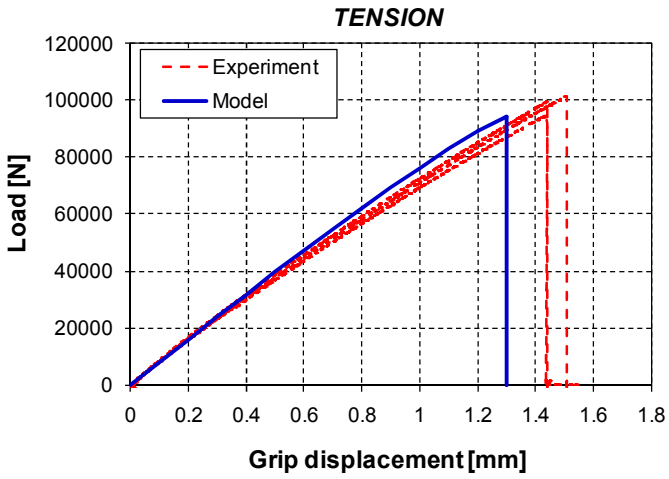

Fig.9: Comparison between experimental and numerical load-displacement curves of the joint for the tension load-case.

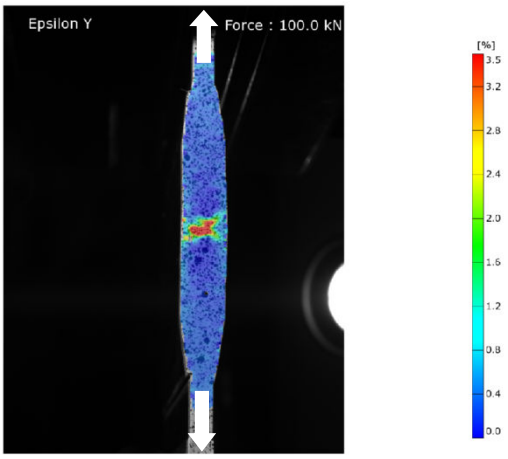

Fig.10: Strain contour in the *Y* direction of the joint subjected to tension, as measured by the ARAMIS system, at final failure.

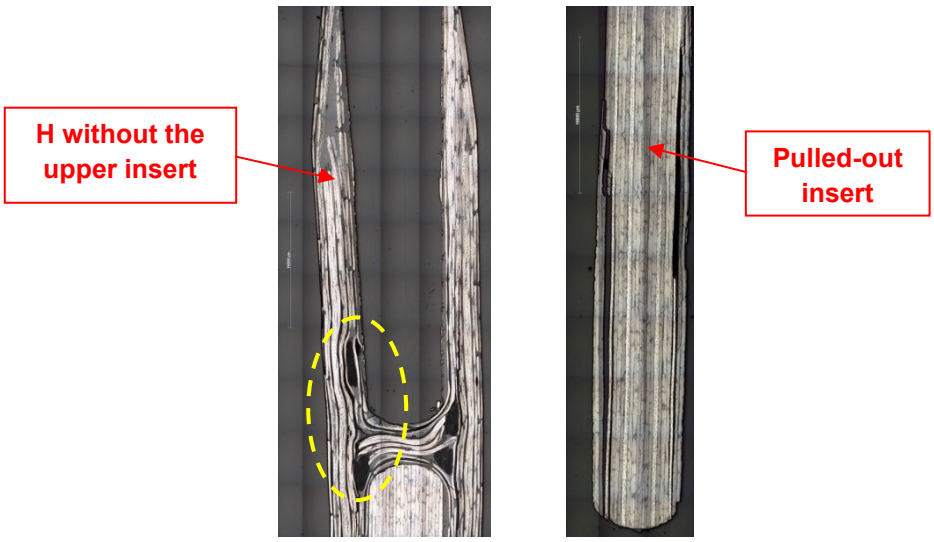

Fig.11: The disassembled joint due to tension.

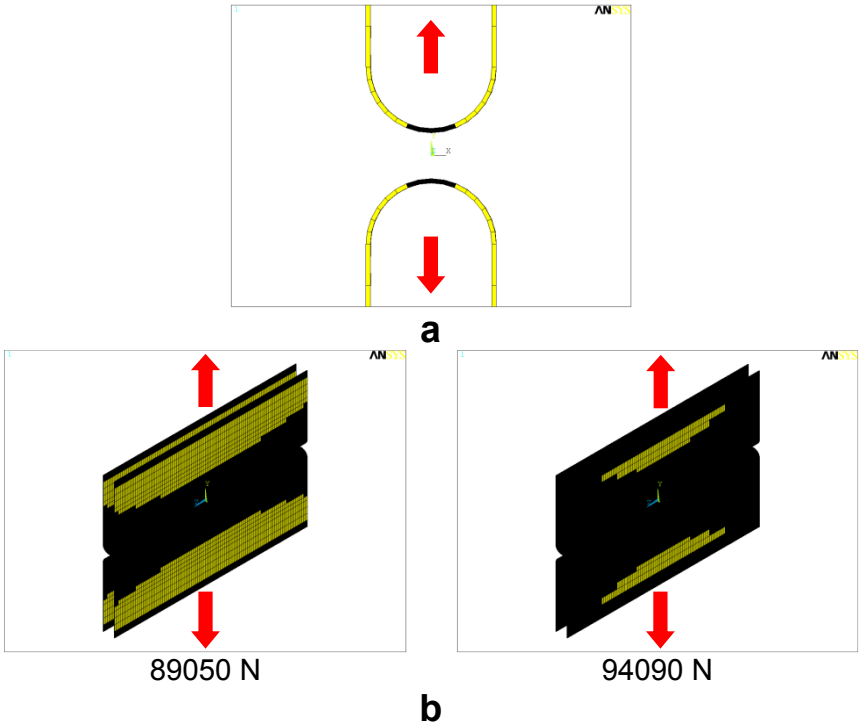

Fig.12: Predicted (a) early debonding initiation (black color) due to tensile fracture and (b) debonding progression due to adhesive shearing up to final failure (94090 N). In the figure, both parts of the adhesive are shown. The arrows indicate the loading direction.

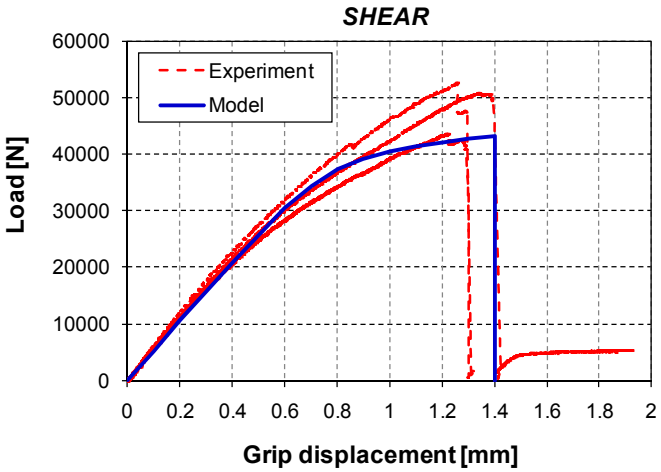

Fig.13: Comparison between experimental and numerical load-displacement curves of the joint for the shear load-case.

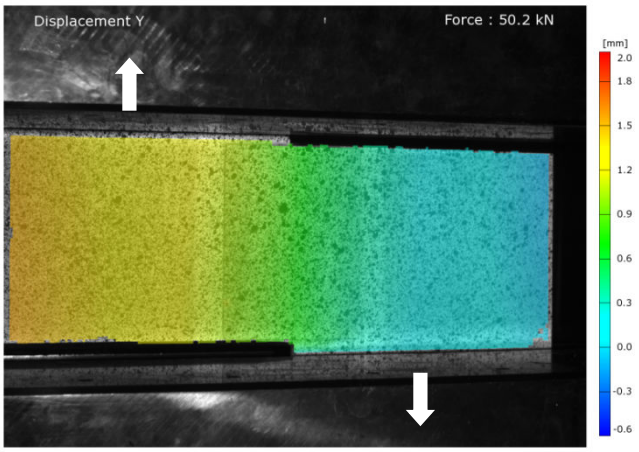

Fig.14: Strain contour in the *Z* direction of the joint subjected to shear, as measured by the ARAMIS system, at final failure.

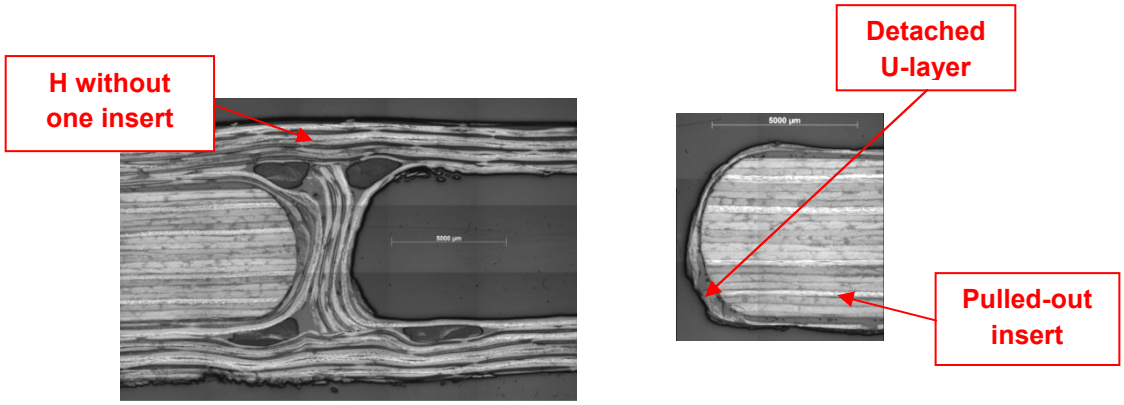

Fig.15: The disassembled joint due to shear.

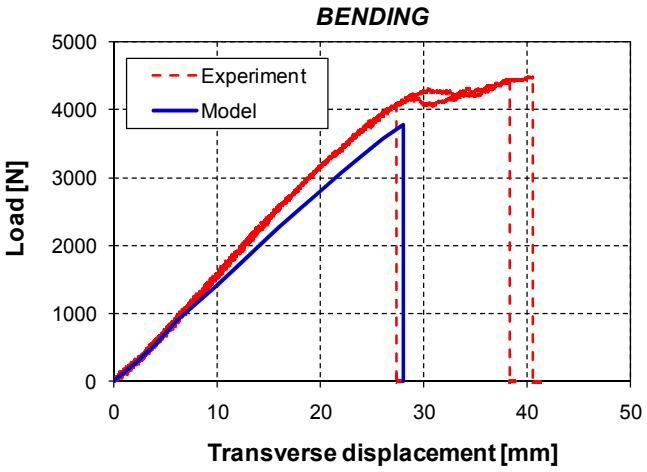

Fig.16: Comparison between experimental and numerical load-displacement curves of the joint for the 4-point bending load-case.

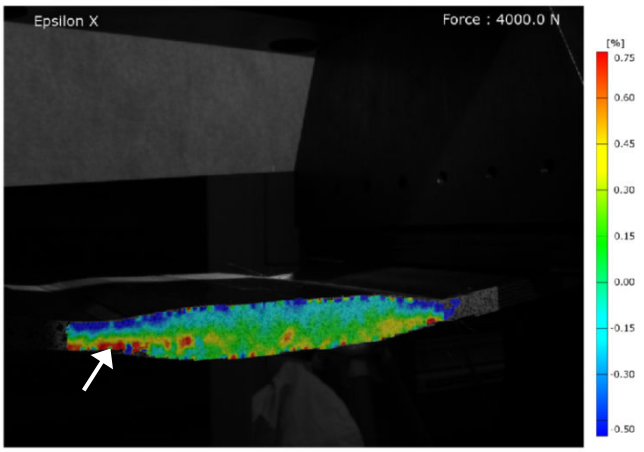

Fig.17: Strain contour in the *X* direction of the joint subjected to 4-point bending, as measured by the ARAMIS system, at final failure.

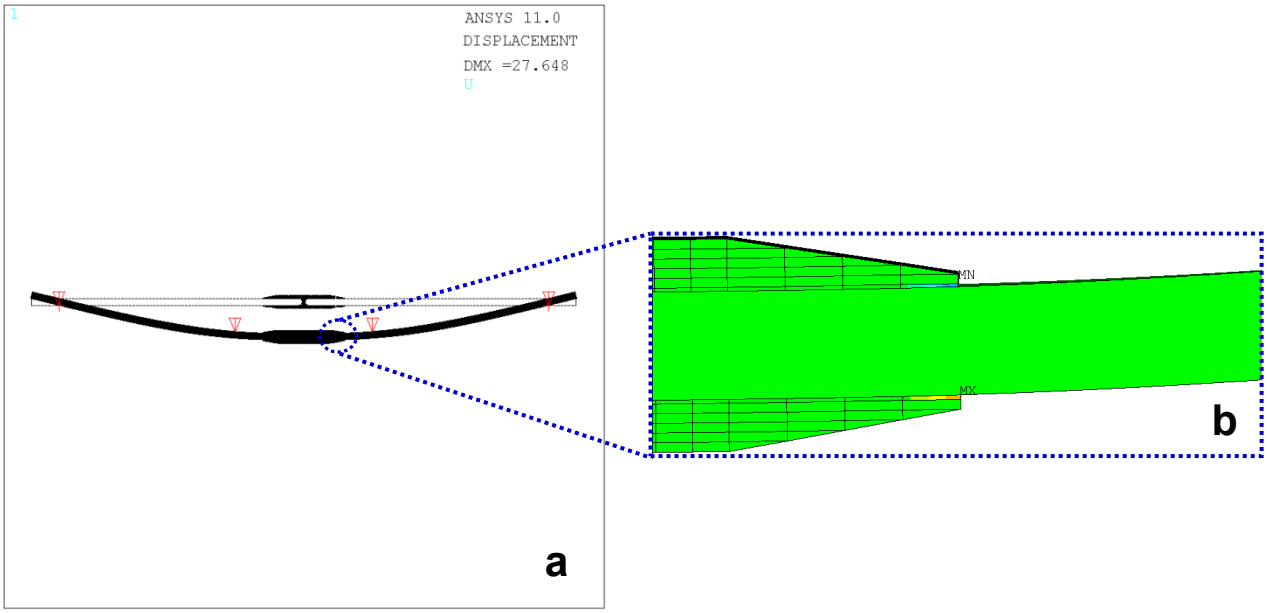

Fig.18: (a) Predicted deformed shape of the joint subjected to 4-point bending. Boundary conditions are indicated with the red arrows. (b) Maximum strain indicating the failure initiation location.

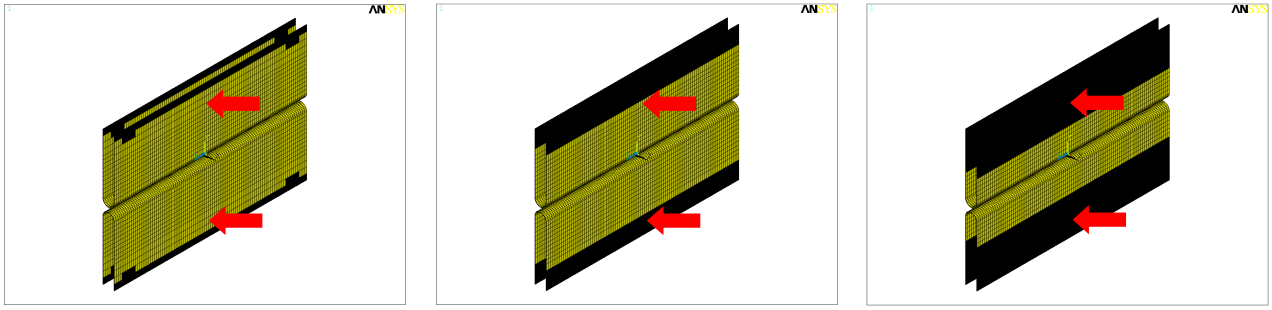

Fig.19: Predicted evolution of debonding as a function of applied load in the joint subjected to 4-point bending.

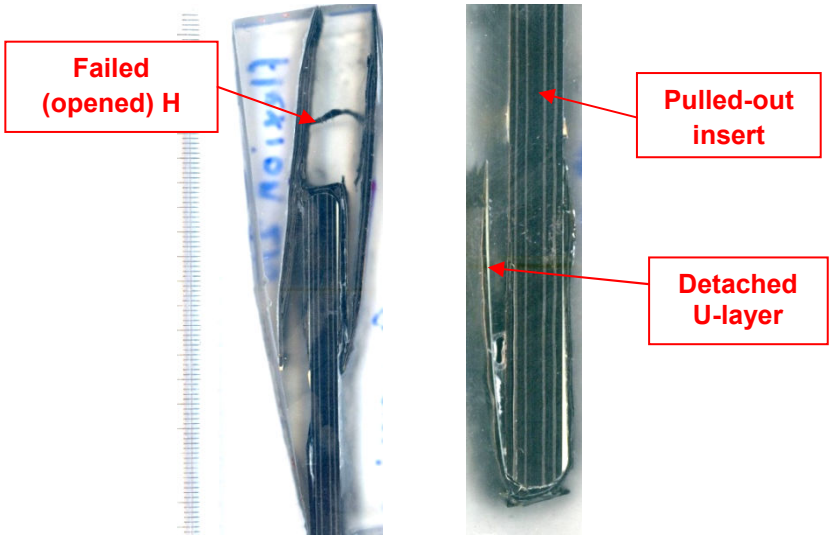

Fig.20: The disassembled joint due to 4-point bending.

Material property	Value
Young's modulus	2548 MPa
Shear modulus	980 MPa
Poisson's ratio	0.3
Shear strength	40 MPa

Table 1: Material properties of the EA 9695 film adhesive.

Loading case	Stiffness [MPa]	Strength [MPa]
Longitudinal tension, *Z*	42930	496
Longitudinal compression, *Z*	47822	692
Transverse tension, *Y*	44158	681
Transverse compression, *Y*	43514	586
Normal tension, *X*	11490	74
Normal compression, *X*	11486	262
In-plane shear, *YZ*	13697	64
Out-of-plane shear, *ZX*	4401	47
Out-of-plane shear, *YX*	4249	47

Table 2: Computed material properties of the NCF HTS/RTM6 quad-layers.

Failed material direction	Degradation rule
Z	$E_X = E_Y = E_Z = G_{XY} = G_{XZ} = G_{YZ} = 0$
Y	$E_X = E_Y = E_Z = G_{XY} = G_{XZ} = G_{YZ} = 0$
X	$E_Z = G_{XZ} = G_{YZ} = 0$
ZY	$G_{YZ} = 0$
ZX	$G_{ZX} = 0$
YX	$G_{YX} = 0$

Table 3: Material property degradation rules.